Onset and cessation of motion in hydrodynamically sheared granular beds

Abram H. Clark, Mark D. Shattuck, Nicholas T. Ouellette, and Corey S. O'Hern

Onset and cessation of motion in hydrodynamically sheared granular beds

Abram H. Clark,[1] Mark D. Shattuck,[2] Nicholas T. Ouellette,[3, 1] and Corey S. O'Hern[1, 4, 5]

[1]*Department of Mechanical Engineering and Materials Science,*
Yale University, New Haven, Connecticut 06520, USA
[2]*Benjamin Levich Institute and Physics Department,*
The City College of the City University of New York, New York, New York 10031, USA
[3]*Department of Civil and Environmental Engineering,*
Stanford University, Stanford, California 94305, USA
[4]*Department of Physics, Yale University, New Haven, Connecticut 06520, USA*
[5]*Department of Applied Physics, Yale University, New Haven, Connecticut 06520, USA*

We performed molecular dynamics simulations of granular beds driven by a model hydrodynamic shear flow to elucidate general grain-scale mechanisms that determine the onset and cessation of sediment transport. By varying the Shields number (the nondimensional shear stress at the top of the bed) and particle Reynolds number (the ratio of particle inertia to viscous damping), we explore how variations of the fluid flow rate, particle inertia, and fluid viscosity affect the onset and cessation of bed motion. For low to moderate particle Reynolds numbers, a critical boundary separates mobile and static states. Transition times between these states diverge as this boundary is approached both from above and below. At high particle Reynolds number, inertial effects become dominant, and particle motion can be sustained well below flow rates at which mobilization of a static bed occurs. We also find that the onset of bed motion (for both low and high particle Reynolds numbers) is described by Weibullian weakest-link statistics, and thus is crucially dependent on the packing structure of the granular bed, even deep beneath the surface.

I. INTRODUCTION

Fluid flowing laterally over a granular bed exerts shear stress on the grains. This occurs in many natural settings and industrial applications, such as sediment transport in riverbeds [1, 2] and slurries pipes [3, 4]. The ratio of the shear stress exerted by the fluid on the top of the bed to the buoyancy-corrected particle weight is known as the Shields number Θ [5]. For small Θ, no grain motion occurs; at sufficiently large Θ, however, grains can be entrained by the flow [6–15]. Despite decades of research, the nature of the transition between static and mobilized granular beds is not well understood. The geometric structure of the contact network in the bed determines its mechanical strength [16–18]. Bed mobilization is also strongly affected by the complex and unsteady fluid flow above the bed, as well as how strongly the fluid flow couples to the grains, as quantified by the particle Reynolds number Re_p [5, 7, 10, 11] that measures how quickly grains equilibrate to the fluid flow. Weak stresses applied to the interior of the bed by fluid flowing through the pore spaces between grains may also play a role in bed mobilization [19–21]. Although empirical hydraulic models capture some important aspects of sediment transport problems [8], there is at present no fundamental understanding of the relative contributions of these effects on the onset and cessation of grain motion.

In this paper, we study a simplified model of a fluid-driven granular bed to clarify the essential physics at the onset of bed motion. In particular, we seek to understand the nature of the mobile-to-static and static-to-mobile transitions as a function of Θ and Re_p and to predict the parameter regime where hysteresis, defined as a finite difference between Θ_0, above which a static bed will begin to move, and Θ_c, below which a mobile system will come to rest, occurs.

We performed molecular dynamics (MD) simulations of a two-dimensional (2D) system composed of frictionless disks subjected to a simplified fluid flow that decays from a large value above the bed to a small value inside the bed. Although our model is highly simplified, with, for example, no explicit unsteadiness in the flow or friction between the grains, we find that $\Theta_c(Re_p)$ from the simulations is consistent with the behavior obtained from a large collection of experiments on sediment transport [7, 10, 11]. In particular, we find plateau values Θ_c^l and Θ_c^h at low and high Re_p, with $\Theta_c^l > \Theta_c^h$, and an intermediate Re_p regime that connects the two limiting values. In the low Re_p limit, there is a sharp transition at Θ_c between mobile and static beds in the infinite-time and infinite-system-size limits with no hysteresis. In the large Re_p limit, we find significant hysteresis, since particle inertia can sustain motion well below the Θ_0 at which bed motion is initiated. We also find that the onset of bed motion at $\Theta > \Theta_c$ for low Re_p and $\Theta > \Theta_0$ for high Re_p depends strongly on system size and exhibits weakest-link statistics [22, 23]. Thus, the onset of bed motion in our system depends on the bed packing structure, even deep beneath the surface.

II. DETAILS OF THE MODEL

We study a domain of width W that contains $N/2$ large and $N/2$ small disks with diameter ratio 1.4. There is no upper boundary, and the lower boundary is rigid with infinite friction so that the horizontal velocities of all particles touching it are set to zero. We use periodic boundary conditions in the horizontal direction. The total force on each particle is given by the vector sum of contact forces from other particles, a gravitational force, and a Stokes-drag-like force from a fluid that moves horizontally:

$$m_i \vec{a}_i = \sum_j \vec{F}_{ij}^c - m_i g' \hat{y} + B_i[v_0 f(\vec{r})\hat{x} - \vec{v}_i]. \quad (1)$$

Here, $m_i \propto D_i^2$ is the particle mass, D_i is the diameter of particle i, $\vec{v}_i$ and $\vec{a}_i$ are the velocity and acceleration of particle i, $m_i g'$ is the buoyancy-corrected particle weight, $B_i \propto D_i$ sets the drag on disk i, v_0 is a characteristic fluid velocity at the surface of a static bed, and $f(\vec{r})$ is the fluid velocity at $\vec{r}$. $\vec{F}_{ij}^c = K \left(1 - \frac{r_{ij}}{D_{ij}}\right) \theta \left(1 - \frac{r_{ij}}{D_{ij}}\right) \hat{r}_{ij}$ is the pairwise repulsive contact force on disk i from disk j, where K is the particle stiffness, r_{ij} is the separation between the centers of the particles, $D_{ij} = (D_i + D_j)/2$, $\hat{r}_{ij}$ is the unit vector connecting their centers, and θ is the Heaviside step function. $f(\vec{r})$, the fluid velocity profile, varies smoothly from a large value above the bed to a small value inside the bed. We choose a form that depends only on the local packing fraction ϕ_i: $f(\phi_i) = e^{-b(\phi_i - 0.5)}$ where b controls the ratio of the magnitude of the fluid flow above and inside the bed. ϕ_i is calculated in a small circular region with diameter $D_i + 2D_l$ around each particle, as shown in Fig. 1(a). We note that $f = 1$ for $\phi_i = 0.5$, a typical value at the bed surface. See Section III A for force profiles in static and mobile states.

Three nondimensional numbers govern the behavior of Eq. (1). We set the nondimensional stiffness $\frac{K}{mg'} > 3 \times 10^3$ to be sufficiently large that increasing it has no effect on our results. The other two nondimensional parameters can be written as

$$\Theta = \frac{Bv_0}{mg'} \quad (2)$$

$$\Gamma = \frac{B/m}{\sqrt{g'/D}}. \quad (3)$$

The Shields number Θ gives the dimensionless shear force at the top of a static bed. Γ is the ratio of the gravitational settling time $\tau_s = \sqrt{D/g'}$ to the viscous time scale m/B. Since the particle Reynolds number $Re_p = \frac{v_0 D}{\nu}$, where ν is the kinematic viscosity, and the Stokes drag is proportional to $\rho_f \nu D$, where ρ_f is the fluid density, the ratio $\frac{\Theta}{\Gamma^2} = \frac{mv_0}{BD} \propto \frac{\rho_g}{\rho_f} Re_p$ (ρ_g is the mass density of the grains) compares the inertia of grains entrained in the flow to the strength of the viscous drag.
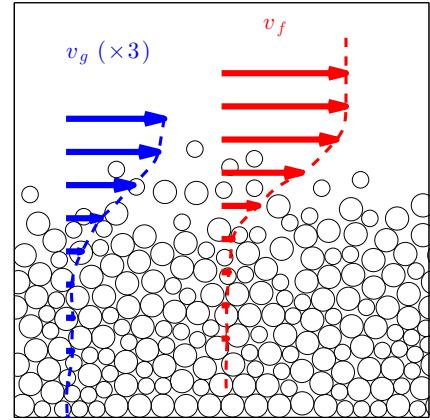
(a)
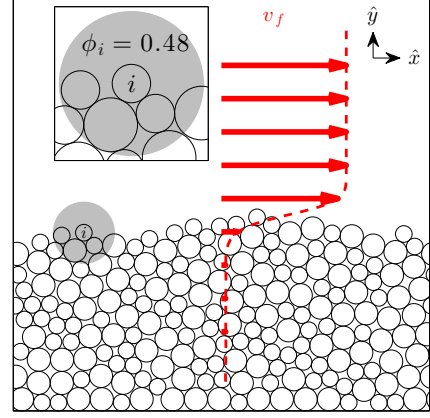
(b)

FIG. 1. (Color online) Layer-averaged fluid velocity v_f versus depth for static (a) and mobile (b) beds. Grains are subjected to a fluid drag force and a gravitational force $-mg'\hat{y}$. The gray circle (left panel) defines the area used to calculate the local packing fraction ϕ_i near the ith particle, which determines the local fluid velocity. We also show the layer-averaged grain velocity v_g for a mobile bed in the right panel.

To characterize flow onset and cessation in our system, we employed two protocols. In protocol A, to study the mobile-to-static transition, we distributed particles randomly throughout the domain and set a constant value of Θ for a total time of roughly $10^5 \tau_s$. We consider the bed to be at rest when the maximum net particle acceleration a_{max} is below a threshold a_{thresh} roughly one order of magnitude smaller than g' and roughly three orders of magnitude smaller than typical values for a moving bed. In protocol B, to understand the dynamics of the static-to-mobile transition, we begin with a static bed from protocol A and slowly increase Θ in increments $\Delta\Theta = 0.01\Theta$. If $a_{max} < a_{thresh}$ after roughly one inter-grain collision time, then Θ is increased. If $a_{max} > a_{thresh}$, we keep Θ constant until $a_{max} < a_{thresh}$. We designate a system as mobile under protocol B with slightly different criteria:

$a_{max}/a_{thresh} > 10$ and $\bar{v}_g > 0.04 V_s$, where $\bar{v}_g$ is the average horizontal velocity of all grains and $V_s = \sqrt{g'D}$ is the settling velocity. These thresholds filter out small rearrangement events, keeping only states with substantial grain motion.

III.   RESULTS AND DISCUSSION

Figure 2 shows the boundaries between mobile and static beds as a function of Θ and Re_p from simulations with $b = 2$, 4, and 6. We find a curve $\Theta_c(Re_p)$ above which the particles are unable to find a stable packing under protocol A. In the low-Re_p limit near Θ_c, grain motion is highly overdamped, and particles do not leave the bed. As Re_p is increased, the inertial effects of mobilized particles striking the bed make finding a stable configuration more difficult, decreasing Θ_c significantly. Figure 2 shows parameter values where grain motion does (blue circles) and does not (green squares) stop under protocol A. We then apply protocol B to stopped systems and find another boundary $\Theta_0(Re_p)$ that specifies when grain flow can be initiated. For low Re_p, $\Theta_0 < \Theta_c$, and bed motion initiated near Θ_0 is temporary. Thus, at low Re_p, permanent grain motion is initiated at Θ_c in the large system limit, as we discuss below. However, in the high-Re_p limit where particle inertia is dominant, we observe significant hysteresis: grain motion is initiated at Θ_0, which is well above the value of Θ_c where mobile particles colliding with the bed can sustain bed motion. We also note that this result is consistent with [24], where, in simulations of Aeolian transport at high Re_p, a significant perturbation or lift force was required near Θ_c to initiate grain motion. Temporary (filled black circles) and permanent (red crosses) motion under protocol B are also marked in Fig. 2. The basic nature of the flow diagram is insensitive to variations in b, although the numerical values for $\Theta_0(Re_p)$ and $\Theta_c(Re_p)$ change. We note the similarities of $\Theta_c(Re_p)$ in Fig. 2 to the experimental and observational data compiled in [7, 10, 11], even though our model is highly simplified. Both display a plateau in the onset value of Θ at low Re_p, a decrease in the onset value at moderate Re_p, and a lower plateau value at high Re_p.

The b parameter sets the ratios between the fluid velocity above the bed (v_a), at the top of a static bed (v_0), and in the bulk of the bed (v_b) where grains are packed densely (at $\phi_i \approx 0.84$). If a grain is well above the bed, $\phi_i \approx 0.1$ (since the grain itself contributes to the local packing fraction), so the ratio of the fluid velocity for this grain to the fluid velocity at the top of an otherwise static bed (where $\phi_i \approx 0.5$ and thus $f = 1$) is $v_a/v_0 \approx e^{0.4b}$. Table I shows the ratios v_a/v_0, v_0/v_b, and v_a/v_b for $b = 2$, 4, and 6. Note that these ratios increase with b, and that varying b changes all ratios simultaneously. Obviously, a fluid flow model with an additional parameter could decouple the v_a/v_0 and v_0/v_b ratios, but the model used here was chosen as a very simple way to interpolate be-
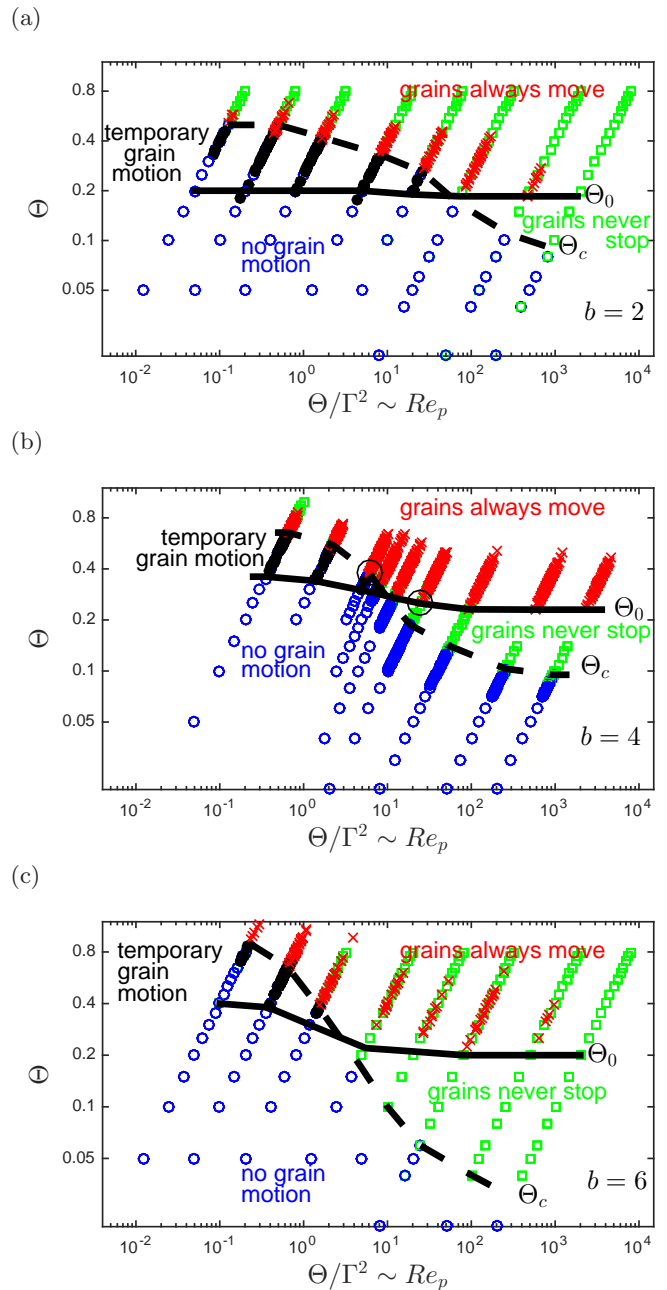

FIG. 2. (Color online) The flow diagrams, Shields number Θ versus particle Reynolds number Re_p, with (a) $b = 2$, (b) $b = 4$, (c) and $b = 6$. Diagonal lines of data points correspond to lines of constant Γ. The symbols show systems that came to rest ($\circ$) or never stopped ($\square$) under protocol A, and were permanently ($\times$) or temporarily ($\bullet$) mobile as Θ was increased under protocol B. The dashed line shows Θ_c, above which inertial effects from particles entrained in the flow lead to sustained motion. The solid line indicates Θ_0, below which the system will never be mobilized. The two large black open circles mark the parameter values we study in Fig. 6.

TABLE I. The flow velocity ratios at different heights and the particle Reynolds number when $\Theta_0 = \Theta_c$. v_a, v_0, and v_b are the fluid velocities above the bed, at the surface of the bed, and in the interior of the bed, respectively.

b	v_a/v_0	v_0/v_b	v_a/v_b	Re_p when $\Theta_0 = \Theta_c$
2	2.23	1.97	4.39	$Re_p \approx 50$
4	4.95	3.89	19.3	$Re_p \approx 10$
6	11.02	7.69	84.8	$Re_p \approx 3$

tween a large fluid velocity above the bed and a small fluid velocity inside the bed. Figure 2 shows that the flow diagram is qualitatively the same for $b = 2$, 4, and 6. Θ_0 is relatively insensitive to b, but Θ_c shifts to smaller Re_p and the gap between the plateau values at large and small Re_p widens with increasing b.

A. Protocol A: Mobile-to-static transition

Figure 3 shows data from protocol A near Θ_c, which we find to be nearly independent of system size, as we discuss below. In Fig. 3(a), we show the time evolution of $\bar{v}_g$ multiplied by the fill height ND/W and normalized by V_s. At short times (red curve), $\bar{v}_g$ increases linearly with Θ and connects continuously to $\bar{v}_g = 0$. This is the expected relation for frictionless granular systems: no motion occurs below the yield stress, while above the yield stress the strain rate increases as a power law in the difference between the applied and yield stresses [25]. However, at long times we observe a discontinuity in $\bar{v}_g$ at Θ_c, as has also been observed in experiments [12] as well as simulations of Aeolian transport [24] and sheared frictional granular media [26]. The discontinuity in $\bar{v}_g$ moves toward Θ_c as time increases. The size of the discontinuity and the slope $\bar{v}_g/\Theta$ both scale roughly linearly with Re_p, as shown in Fig. 3(b). For Shields numbers below Θ_c, the grains settle into a stable packing in a time t_s that diverges as $\Theta \rightarrow \Theta_c$, as shown in Fig. 3(c).

Figure 1 shows that mobile grains are confined to a relatively small layer at the top of the bed. So, for fill heights studied here ($ND/W > 8$), we find the total flow rate $\bar{v}_g ND/W$ as a function of Θ and Γ is insensitive to the system size (recall, $\bar{v}_g$ is the average velocity of all grains). One might think that the discontinuity in the the flow rate near Θ_c may disappear in the large-system limit: small systems of grains are able to find a stable configuration, but very large systems will always have a weak spot that does not allow the system to stop. However, this is not the case. Figure 3(d) shows that the behavior near $\Theta = \Theta_c$ is insensitive to the system size. The stopping time as a function of Θ is shown for three different system sizes, and the three curves are virtually identical. The mean and fluctuations of the stopping time both diverge as a power law as $\Theta \rightarrow \Theta_c$. The data shown is for $\Gamma = 0.24$ and $b = 4$, where $\Theta_c > \Theta_0$, and the power law exponent is roughly 2.5. As shown in Fig. 3(c),
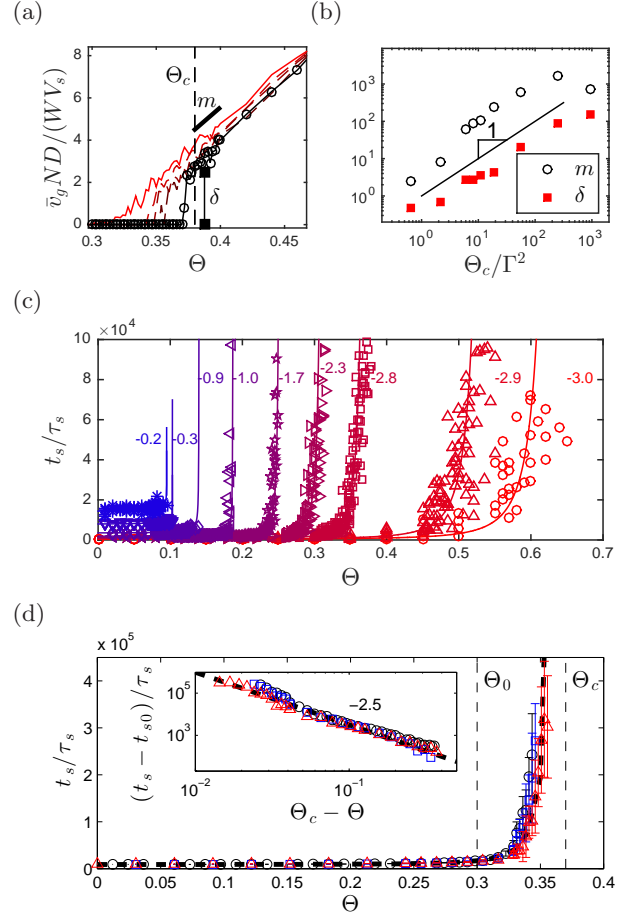

FIG. 3. (Color online) Data from protocol A near Θ_c. (a) Time evolution of the average grain velocity $\bar{v}_g(t)$ during protocol A. The solid red curve characterizes grain motion at the time for grains to settle under no fluid flow t_{s0}, the black curve with open circles marks the end of the simulation, and dashed curves represents intermediate times (where red to black represents increasing time). At long times, we observe a discontinuity in $\bar{v}_g$ with magnitude δ and slope m at Θ_c. (b) δ and m scale roughly linearly with Re_p. (c) The time t_s required for the grains to come to rest as a function of Θ for varying Re_p (left to right, blue to red, represents large to small Re_p); symbols show $\Gamma = 0.01$ (∗), 0.02 (▽), 0.05 (◇), 0.1 (◁), 0.15 (⋆), 0.2 (▷), 0.25 (□), 0.5 (△), and 1 (○). The lines show fits of $(t_s - t_{s0}) \propto (\Theta_c - \Theta)^\alpha$, where the values of α are marked next to each plot. (d) t_s is plotted as a function Θ for $b = 4$, $\Gamma = 0.24$, and three system sizes. The symbols correspond to $(W/D, N)$: black circles (100,800), blue squares (50,400), and red triangles (50,800). Data points show the mean of ten simulations, and error bars give the standard deviation. The inset shows a logarithmic plot of the mean of $t_s - t_{s0}$. The thick dashed line corresponds to $(t_s - t_{s0}) \propto (\Theta_c - \Theta)^{-2.5}$.

this exponent is roughly 3 in the low Re_p limit, and it decreases with increasing Re_p to less than 1 in the high Re_p limit. Θ_0 is also shown, and it corresponds reasonably well to where the divergence begins, which suggests that $\Theta_c - \Theta_0$ is related to the power law exponent of the divergence.
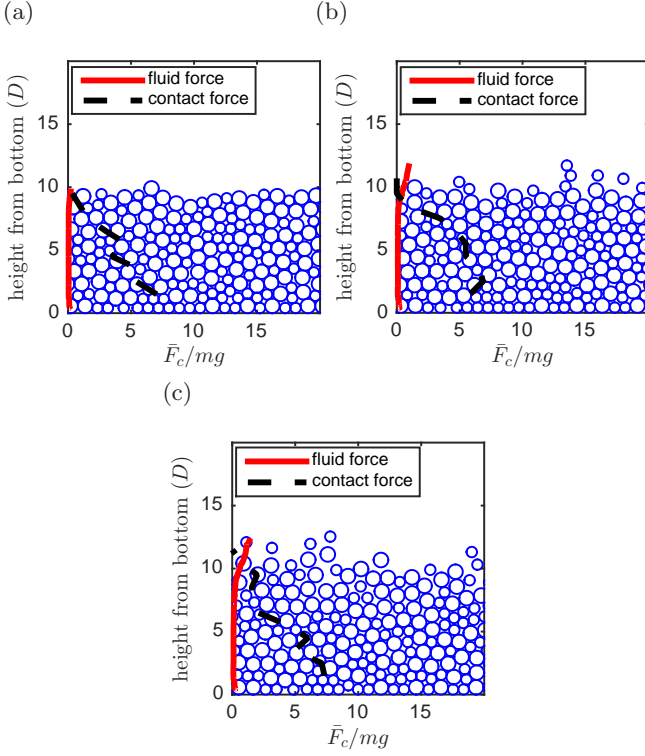
FIG. 4. (Color online) Profiles of the layer-averaged instantaneous fluid drag force (red lines) and the local pressure (black dashed lines) for $b = 4$ and $\Gamma = 0.25$, with (a) $\Theta = 0.2$, (b) 0.35, and (c) 0.4.

In Figure 4, we show typical force profiles during protocol A for grains under three different conditions. All panels have $b = 4$ and $\Gamma = 0.25$, but with varying Θ. Solid red curves show the average force exerted by the fluid on the grains at a particular height. Black dashed curves show the average pressure due to grain-grain contacts as a function of height. To calculate the pressure, we first calculate the force moment tensor $M_{\alpha\beta}^i$ at particle i by summing over the particles j that contact particle i to obtain $M_{\alpha\beta}^i = \frac{1}{R_i} \sum_j F_\alpha^{ij} r_\beta^{ij}$, where R_i is the particle radius, α and β represent components, and r_β^{ij} represents the β component of the branch vector connecting the center of particle i with the point of contact with particle j. The mean of the eigenvalues of this tensor provides a grain-scale estimate of the local pressure, which we then average over the horizontal direction to obtain the average contact force $\bar{F}_c$. We plot $\bar{F}_c$ in Fig.4 as a function of height from the lower boundary as a black dashed line, which has roughly slope 1 in all plots. Thus, the contact forces below the surface are dominated by the weight of grains above a particular layer. Figure 4(a) shows $\Theta = 0.2$, which is below both Θ_0 and Θ_c, so grains are not moving. Figure 4(b) shows $\Theta = 0.35$, so the flow is metastable and grains will eventually come to a stop. Figure 4(c) shows $\Theta = 0.4$, so grains continue to move indefinitely.

B. Protocol B: Static-to-mobile transition

For $\Theta > \Theta_c$, a sufficiently large perturbation will lead to sustained bed motion. At high Re_p, this motion never begins for $\Theta < \Theta_0$. But as the red crosses in Fig. 2 show, stable motion is not always initiated at these minimum values, but depends on the particular arrangement of grains in the bed. We show that sustained grain motion is consistent with Weibullian weakest link statistics [22, 23] and that failure events are always initiated at Θ_c for low Re_p and Θ_0 for high Re_p for sufficiently large systems.

First, we note that although the first large-scale motion of the grains always occurs at the top layer of grains, failure events do not always originate there. If we measure the depth of the particle whose acceleration first exceeds a_thresh at Θ_f, we find that it can occur at any depth y_f below the bed surface, with a probability distribution p_f that is proportional to the local applied fluid force as shown in Fig. 5. Essentially, the ratio of the probability of failure at the surface to the probability of failure in the bed is roughly given by the ratio between the fluid force at the top of the bed to that inside the bed v_0/v_b, as given in Table I. Thus, while large-scale particle motion always begins at the surface of the bed, this motion is often correlated to small particle rearrangements that occur deep in the bed.

Figure 6(a) and (d) show that the probability distribution $P(\Theta_f)$ approaches $\delta(\Theta_f - \Theta_c)$ for low Re_p and $\delta(\Theta_f - \Theta_0)$ for high Re_p in the large system limit, where we varied both N and W to change the system size. The insets show that the distributions $P(\Theta_f)$ collapse when rescaled by their mean values. The system-size dependence suggests a "weakest link" picture: at a given value of excess stress above Θ_c or Θ_0 (for low and high Re_p, respectively), there is a better chance of finding a sufficiently weak local grain arrangement somewhere in a larger system. If we consider the bed to be a composite system of M *uncorrelated* subsystems that fails if any of the subsystems fail, the cumulative distribution $C_M(\Theta)$ for failure is related to that of a single subsystem $C(\Theta)$ by

$$1 - C_M(\Theta) = [1 - C(\Theta)]^M . \tag{4}$$

If we assume a Weibull distribution [22, 23, 27]

$$C(\Theta) = 1 - \exp\left[\left(\frac{\Theta - \Theta_c}{\beta}\right)^\alpha\right], \tag{5}$$

then $C_M(\Theta)$ will have the same form with $\alpha_M = \alpha$ and $\beta_M = \beta M^{-1/\alpha}$. Figure 6(a) and (d) show that $P(\Theta_f) = dC/d\Theta_f$ does indeed obey a Weibull distribution with shape parameter $\alpha \approx 2.6$.

Thus, if Eq. (5) fits the data, and if α is constant but $\beta \propto M^{-1/\alpha}$ as M is varied, then Eq. (4) applies, and global failure is caused by the failure of a single member of a collection of uncorrelated subsystems. Figure 6(b) and (e) confirm this, showing that the mean Shields number at flow onset $\bar{\Theta}_f$ scales as $(\bar{\Theta}_f - \Theta_c) \propto M_\text{eff}^{-1/\alpha}$ for
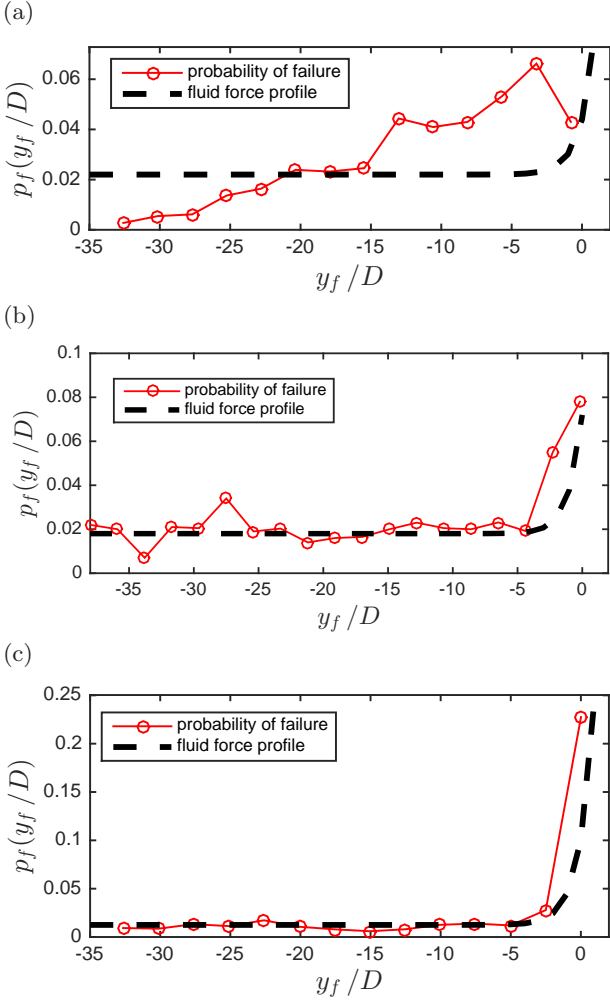
(a)

(b)

(c)

FIG. 5. (Color online) The probability p_f that bed failure occurs at depth y_f (where $y_f = 0$ is the top of the bed) is proportional to the local fluid force for (a) $b = 2$ and $\Gamma = 0.1$, (b) $b = 4$ and $\Gamma = 0.25$, and (c) $b = 6$ and $\Gamma = 0.5$. The bed failure depth is determined as the depth of the particle whose acceleration first exceeds a_{thresh} (or a weighted average of depths, if multiple grains meet this condition simultaneously). The agreement between $p_f(y_f)$ and the local fluid force is good for $b = 4$ and 6 cases, but there is a deviation for the $b = 2$ case, such that p_f is smaller than expected near the lower boundary and bed surface. One explanation for this is that failure events are less localized, causing the weighted average of $a_i > a_{\mathrm{thresh}}$ to be more likely in the middle of the system.

small Re_p and $(\bar{\Theta}_f - \Theta_0) \propto M_{\mathrm{eff}}^{-1/\alpha}$ for large Re_p, where $M_{\mathrm{eff}} = W_{\mathrm{eff}} H_{\mathrm{eff}}/D^2$ is the effective system size. This scaling means that larger systems are more likely to fail near Θ_c or Θ_0 for small and large Re_p, respectively. However, systems that fail near these minimum values are very slow to become fully mobilized. To demonstrate this, we consider the mobilization time t_m, defined as the time between the initial force imbalance that leads to failure and the time when $\bar{v}_g$ reaches its asymptotic value. As shown in Fig. 6(c) and (f), this time scale also

diverges as $\Theta \to \Theta_c$ for low Re_p and $\Theta \to \Theta_0$ for high Re_p, and is independent of system size.

To calculate M_{eff}, we determine W_{eff} and H_{eff} as follows. Since the vertical symmetry is broken by the fluid forcing profile, we calculate H_{eff} by integrating the probability of failure over the depth of the system, which is equal to the fluid force profile. That is, H_{eff} is the integral of the profiles shown in Fig. 5 over the depth of the bed, since the relevant system size for the Weibullian weakest link scaling has to do with the probability of local failure, and, as previously mentioned, particles near the surface cause failure with a likelihood that is greater than particles beneath the surface by a factor v_0/v_b. We find that this form for H_{eff} collapses the data for systems that are sufficiently large in the horizontal (periodic) direction. We also check the form of H_{eff} for a case where $b = 2$ and $\Gamma = 0.1$, such that $v_0/v_b \approx 1.97$, and we find it to collapse the data well according to the Weibullian scaling. The form of H_{eff} confirms our observation that surface grain motion can be initiated from deep beneath the surface, as it is also proportional to the local applied shear force.

The horizontal dimension is symmetric, but we find finite system-size effects when $W/D < \xi$, where ξ is a horizontal correlation length that varies with Re_p. As shown in Fig. 6, we find $M_{\mathrm{eff}} = 0.91(\bar{\Theta}_f - \Theta_c)^{-\alpha}$ for large systems, where H_{eff} is calculated using the method described previously. However, when the horizontal dimension becomes small, we observe that $(\bar{\Theta}_f - \Theta_c)$ is larger than expected, which corresponds to an effective system width W_{eff} that is smaller than the real system width W.

If $M_{\mathrm{eff}} = 0.91(\bar{\Theta}_f - \Theta_c)^{-\alpha} = H_{\mathrm{eff}} W_{\mathrm{eff}}/D^2$, and we assume that $W_{\mathrm{eff}}/W = \zeta(W/D)$, then we can write

$$\zeta(W/D) = 0.91(\bar{\Theta}_f - \Theta_c)^{-\alpha} \frac{D^2}{H_{\mathrm{eff}} W}. \qquad (6)$$

A plot of this quantity is shown in Fig. 7, and the fit line corresponds to

$$\zeta(W/D) = 1 - \exp\left[-\frac{W}{\xi D}\right]. \qquad (7)$$

As Fig. 7 shows, the form $W_{\mathrm{eff}}/W = 1 - \exp\left[-\frac{W}{\xi D}\right]$ captures the finite size effects. We find a similar result for the the high Re_p case in Fig. 6(d)-(f), where $\Gamma = 0.1$ and $b = 4$, but with a smaller value of $\xi \approx 3$. The form of W_{eff} suggests a horizontal correlation length of roughly ξ, which is larger for low Re_p ($\xi \approx 17$) than for high Re_p ($\xi \approx 3$).

IV. SUMMARY

In summary, we performed numerical simulations of a granular bed subjected to a simple fluid shear flow to understand general features of the initiation and cessation of grain motion. The critical Shields number for the
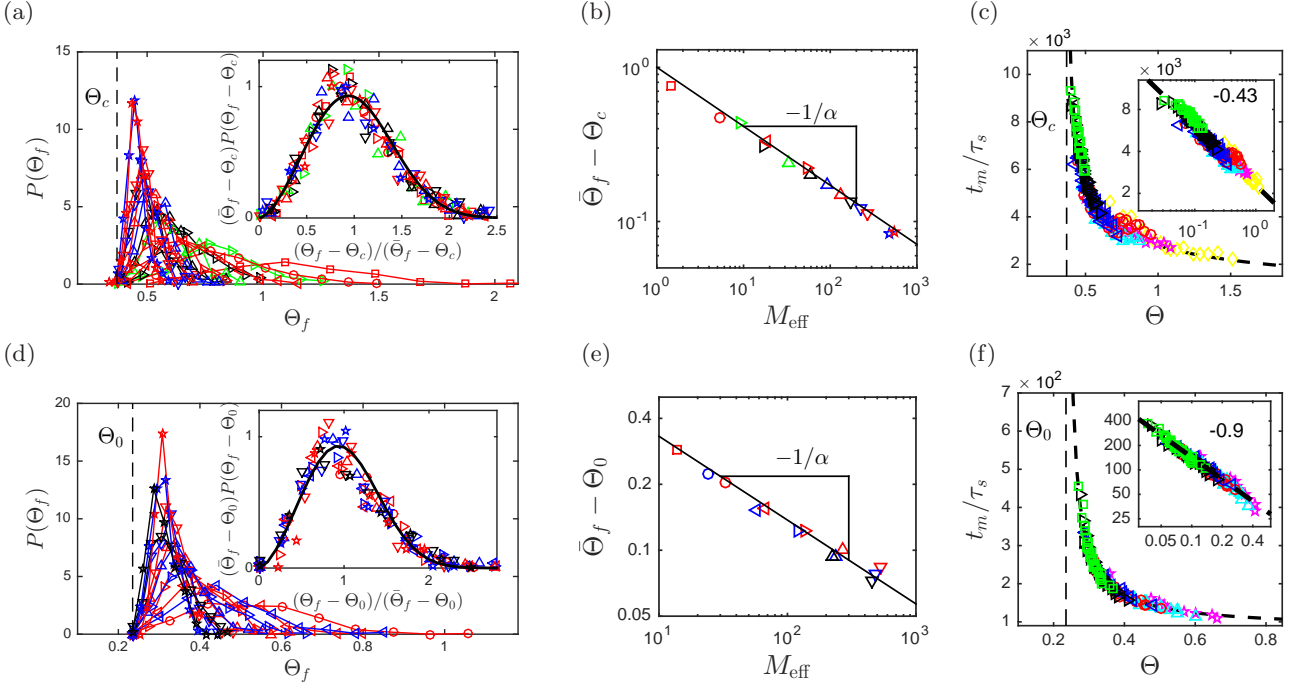
FIG. 6. (Color online) Onset of bed motion is governed by Weibullian weakest-link statistics. (a)-(c) correspond to low Re_p with $\Gamma = 0.25$ and (d)-(f) correspond to high Re_p with $\Gamma = 0.1$. (a) and (d) show the probability distribution of the Shields number at bed failure Θ_f for many different system sizes (W/D from 3.125 to 200, N from 25 to 1600, and WN/D from 8 to 80). The dashed vertical lines define (a) Θ_c and (d) Θ_0. The insets show that $P(\Theta_f)$ collapses when rescaled by $\bar{\Theta}_f - \Theta_c$, where $\bar{\Theta}_f$ is the mean of each distribution. The solid line is a Weibull distribution with shape parameter $\alpha \approx 2.6$. (b) and (e) indicate that $\bar{\Theta}_f - \Theta_c$ for low Re_p and $\bar{\Theta}_f - \Theta_0$ for high Re_p scale with the effective system size $M_{\mathrm{eff}}^{-1/\alpha}$. (c) and (f) show that t_m, the mobilization time after bed failure, diverges near Θ_c and Θ_0, respectively, independent of system size. The insets show a logarithmic plot of $t_m - t_{m,0}$ versus (c) $\Theta - \Theta_c$ and (f) $\Theta - \Theta_0$. The dashed lines show $t_m - t_{m,0} \propto (\Theta - \Theta_c)^{-0.43}$ (c) and $t_m - t_{m,0} \propto (\Theta - \Theta_c)^{-0.9}$ (f), and the thin vertical dashed line indicates Θ_c. Symbols ($\diamond, \star, \triangle, \circ, \triangleleft, \triangleright, \square$) correspond to different values of N (25, 50, 100, 200, 400, 800, and 1600, respectively) with varying W/D. Each data point represents an average of 20 simulations.
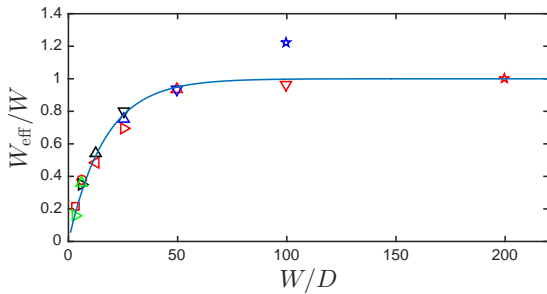

FIG. 7. (Color online) This plot shows the finite system size effects in the horizontal periodic direction (with $b = 4$ and $\Gamma = 0.25$, which are the same values for the low Re_p data shown in Fig. 6(a)-(c)). The horizontal axis is the system width in particle diameters, W/D. As we show in in Fig. 6(a)-(c), we find $M_{\mathrm{eff}} = 0.91(\bar{\Theta}_f - \Theta_c)^{-\alpha}$ for large systems. The vertical axis shows this quantity, $0.91(\bar{\Theta}_f - \Theta_c)^{-\alpha}$, divided by the product of the effective fill height H_{eff}/D and the width in particle diameters W/D. This shows a good collapse, and the fit line corresponds to $W_{\mathrm{eff}}/W = 1 - \exp\left[-\frac{W}{\xi D}\right]$, with $\xi = 16.7$, and 95% confidence interval of roughly $15 < \xi < 20$.

onset of grain motion $\Theta_c(Re_p)$ from the simulations is consistent with the behavior from a large body of experimental results [7]. At low Re_p, $\Theta_c(Re_p)$ separates mobile and static beds, but at high Re_p, we observe significant hysteresis as a consequence of particle inertia. We find that the onset of grain motion is directly connected to the packing structure, even deep in the bed where there is a weak but nonzero fluid stress [19–21]. Our results from this simple model clarify the essential physics governing the transition between mobile and static beds. In future work, additional effects such as turbulent flow, inter-grain friction, and nontrivial particle shape can be added one-by-one to determine their distinct effects on the onset and cessation of grain motion.

[1] H. A. Einstein, *The Bed-load Function for Sediment Transportation in Open Channel Flows*, Technical bulletin (United States. Dept. of Agriculture) (U.S. Department of Agriculture, 1950).

[2] Franois Charru, Bruno Andreotti, and Philippe Claudin, "Sand ripples and dunes," Annual Review of Fluid Mechanics **45**, 469–493 (2013).

[3] P. Doron, D. Granica, and D. Barnea, "Slurry flow in horizontal pipesexperimental and modeling," International Journal of Multiphase Flow **13**, 535 – 547 (1987).

[4] J. Capecelatro and O. Desjardins, "Eulerian–Lagrangian modeling of turbulent liquid-solid slurries in horizontal pipes," Intl. J. Multiphase Flow **55**, 64–79 (2013).

[5] A. Shields, "Anwendung der ähnlichkeitsmechanik und der Turbulenzforschung auf die Geschiebebewegung," in *Mitteilungen der Preussischen Versuchsanstalt für Wasserbau und Schiffbau*, Vol. 26 (1936).

[6] Patricia L. Wiberg and J. Dungan Smith, "Calculations of the critical shear stress for motion of uniform and heterogeneous sediments," Water Resources Research **23**, 1471–1480 (1987).

[7] J. M. Buffington and D. R. Montgomery, "A systematic analysis of eight decades of incipient motion studies, with special reference to gravel-bedded rivers," Water Resour. Res. **33**, 1993–2029 (1997).

[8] F. Charru, H. Mouilleron, and O. Eiff, "Erosion and deposition of particles on a bed sheared by a viscous flow," J. Fluid Mech. **519**, 55–80 (2004).

[9] Malika Ouriemi, Pascale Aussillous, Marc Medale, Yannick Peysson, and lisabeth Guazzelli, "Determination of the critical shields number for particle erosion in laminar flow," Physics of Fluids **19**, 061706 (2007).

[10] A.A. Beheshti and B. Ataie-Ashtiani, "Analysis of threshold and incipient conditions for sediment movement," Coastal Engineering **55**, 423 – 430 (2008).

[11] Subhasish Dey and Athanasios Papanicolaou, "Sediment threshold under stream flow: A state-of-the-art review," KSCE Journal of Civil Engineering **12**, 45–60 (2008).

[12] E. Lajeunesse, L. Malverti, and F. Charru, "Bed load transport in turbulent flow at the grain scale: Experiments and modeling," J. Geophys. Res. **115**, F04001 (2010).

[13] J. J. Derksen, "Simulations of granular bed erosion due to laminar shear flow near the critical shields number," Physics of Fluids **23**, 113303 (2011).

[14] A. Hong, M. Tao, and A. Kudrolli, "Onset of erosion of a granular bed in a channel driven by fluid flow," Phys. Fluids **27**, 013301 (2015).

[15] M. Houssais, C. P. Ortiz, D. J. Durian, and D. J. Jerolmack, "Onset of sediment transport is a continuous transition driven by fluid shear and granular creep," Nat. Commun. **6**, 7527 (2015).

[16] Leonardo E. Silbert, Deniz Ertaş, Gary S. Grest, Thomas C. Halsey, and Dov Levine, "Geometry of frictionless and frictional sphere packings," Phys. Rev. E **65**, 031304 (2002).

[17] Pierre-Emmanuel Peyneau and Jean-Noël Roux, "Frictionless bead packs have macroscopic friction, but no dilatancy," Phys. Rev. E **78**, 011307 (2008).

[18] Carl F. Schreck, Ning Xu, and Corey S. O'Hern, "A comparison of jamming behavior in systems composed of dimer- and ellipse-shaped particles," Soft Matter **6**, 2960–2969 (2010).

[19] H. E. Rose, "On the resistance coefficientreynolds number relationship for fluid flow through a bed of granular material," Proceedings of the Institution of Mechanical Engineers **153**, 154–168 (1945), http://pme.sagepub.com/content/153/1/154.full.pdf+html.

[20] Gordon S. Beavers and Daniel D. Joseph, "Boundary conditions at a naturally permeable wall," Journal of Fluid Mechanics **30**, 197–207 (1967).

[21] A. E. Scheidegger, *The physics of flow through porous media* (University of Toronto Press, 1974).

[22] W. Weibull, *A Statistical Theory of the Strength of Materials*, Ingeniörsvetenskapsakademiens handlingar (Generalstabens litografiska anstalts förlag, 1939).

[23] W. Weibull, "A statistical distribution function of wide applicability," J. Appl. Mech. **18**, 293–297 (1951).

[24] M. V. Carneiro, T. Pähtz, and H. J. Herrmann, "Jump at the onset of saltation," Phys. Rev. Lett. **107**, 098001 (2011).

[25] Ning Xu and Corey S. O'Hern, "Measurements of the yield stress in frictionless granular systems," Phys. Rev. E **73**, 061303 (2006).

[26] Michio Otsuki and Hisao Hayakawa, "Critical scaling near jamming transition for frictional granular particles," Phys. Rev. E **83**, 051301 (2011).

[27] Scott V. Franklin, "Extensional rheology of entangled granular materials," EPL (Europhysics Letters) **106**, 58004 (2014).